Localization of drug biodistribution in a 3D-bioengineered subcutaneous neovascularized microenvironment

Simone Capuani [a,b], Nathanael Hernandez [a], Jesus Paez-Mayorga [a,c], Prashant Dogra [d,e], Zhihui Wang [d,e,f], Vittorio Cristini [d,e,f,g], Corrine Ying Xuan Chua [a], Joan E. Nichols [h,i], Alessandro Grattoni [a,i,j,*]

[a] Department of Nanomedicine, Houston Methodist Research Institute, Houston, TX, USA
[b] University of Chinese Academy of Science (UCAS), 19 Yuquan Road, Beijing 100049, China
[c] School of Medicine and Health Sciences, Tecnologico de Monterrey, Monterrey, NL, Mexico
[d] Mathematics in Medicine Program, Houston Methodist Research Institute, Houston, TX, 77030, USA
[e] Department of Physiology and Biophysics, Weill Cornell Medical College, New York, NY, 10022, USA
[f] Neal Cancer Center, Houston Methodist Research Institute, Houston, TX, 77030, USA
[g] Department of Imaging Physics, University of Texas MD Anderson Cancer Center, Houston, TX, 77230, USA
[h] Center for Tissue Engineering, Houston Methodist Research Institute, Houston, TX, USA
[i] Department of Surgery, Houston Methodist Hospital, Houston, TX, USA
[j] Department of Radiation Oncology, Houston Methodist Hospital, Houston, TX, USA

ARTICLE INFO

ABSTRACT

Local immunomodulation has shown the potential to control the immune response in a site-specific manner for wound healing, cancer, allergy, and cell transplantation, thus abrogating adverse effects associated with systemic administration of immunotherapeutics. Localized immunomodulation requires confining the biodistribution of immunotherapeutics on-site for maximal immune control and minimal systemic drug exposure. To this end, we developed a 3D-printed subcutaneous implant termed 'NICHE', consisting of a bioengineered vascularized microenvironment enabled by sustained drug delivery on-site. The NICHE was designed as a platform technology for investigating local immunomodulation in the context of cell therapeutics and cancer vaccines. Here we studied the ability of the NICHE to localize the PK and biodistribution of different model immunomodulatory agents in vivo. For this, we first performed a mechanistic evaluation of the microenvironment generated within and surrounding the NICHE, with emphasis on the parameters related to molecular transport. Second, we longitudinally studied the biodistribution of ovalbumin, cytotoxic T lymphocyte-associated antigen-4-Ig (CTLA4Ig), and IgG delivered locally via NICHE over 30 days. Third, we used our findings to develop a physiologically-based pharmacokinetic (PBPK) model. Despite dense and mature vascularization within and surrounding the NICHE, we showed sustained orders of magnitude higher molecular drug concentrations within its microenvironment as compared to systemic circulation and major organs. Further, the PBPK model was able to recapitulate the biodistribution of the 3 molecules with high accuracy (r > 0.98). Overall, the NICHE and the PBPK model represent an adaptable platform for the investigation of local immunomodulation strategies for a wide range of biomedical applications.

1. Introduction

Modulation of the immune system is widely employed in various medical applications, including the management of foreign body response, enhancement of tissue repair and regeneration, and abrogation of transplant rejection. Conventional immunomodulatory strategies

---

hinge on lifelong systemic administration of therapeutics, resulting in whole-body drug exposure, which is often associated with side effects and increased risks of different diseases and opportunistic infections [1–4]. These adverse effects and risks may cause poor quality of life and affect therapeutic adherence, which ultimately hinders efficacy [5,6].

To address these challenges, localized immunomodulating strategies are emerging as attractive alternatives for the treatment of various conditions [7–10]. In this context, a wide array of technologies have been explored for cell transplantation [7,11], wound healing [12–14], cancer vaccines [15–18] and allergy treatment [19,20], among others. Nanoparticle constructs have been developed to achieve drug localization from systemic administration and reduce systemic drug exposure via active molecular targeting [21–23]. However, in most cases, less than 5% of the drug reaches the intended target due to the challenges of breaching through biological barriers [24]. The use of micro-nanocarriers, such as microparticles, micelles or liposomes, paired with localized delivery, has shown enhancement of drug localization and therapeutic index, whilst reducing their circulating levels [25–27]. However, drug release from these platforms is usually exhausted within days [28,29], and maintenance of long-term treatment would require frequent administrations, which limits their applicability. Immunomodulatory hydrogel and implantable scaffolds have also been developed and functionalized with immunomodulating molecules [14,30,31] to control the immune system in various settings [32]. While these provide longer-acting drug release, no mechanism is available to extend release from these systems upon drug exhaustion, requiring replacement or de novo administration. Similar considerations apply for non-refillable reservoir-based implantable devices, which can extend delivery of therapeutic on site via nanofluidic membranes for months [33,34], yet are unable to fulfill the delivery requirements for chronic applications. Overall, these strategies show favorable outcomes in the short term. However, they are largely inadequate in providing a long-lasting immunomodulatory effect due to drug depletion, pointing towards the need for replenishable platforms [35,36]. Further, and equally significant, spatiotemporal assessment of the local biodistribution of immunomodulatory drug from these systems and their resulting immunomodulatory effect in situ is challenging. For these reasons, these technologies are unsuitable for the investigation of novel local immunomodulatory approaches.

To this end, we developed a 3D-printed implantable system termed 'NICHE'. Upon engraftment, the NICHE hosts a spatially-defined bioengineered vascularized microenvironment, which can be manipulated through sustained and transcutaneously replenishable delivery of molecules on-site. The NICHE was conceived as a platform technology for investigating local immunomodulation in the context of cell therapeutics [37–39] and cancer vaccines [16]. The NICHE consists of 2 compartments: a vascularized tissue reservoir and a surrounding refillable drug reservoir [40]. The compartments are separated by a nanoporous membrane that allows controlled elution of immunomodulatory agents from the drug reservoir to the cell reservoir. The latter is enclosed by 2 nylon meshes that allow for tissue and capillaries ingrowth. We previously showed this local delivery platform to maintain viability, function and retention of allogeneic cell grafts (Leydig cells and pancreatic islets) in immunocompetent rats without the need for systemic immunesuppression [37,38].

While we aim to employ NICHE to house transplanted insulin producing cells, such as pancreatic islets or stem cells derived beta cells for the treatment of type 1 diabetes, NICHE-like platforms are applicable to a broad spectrum of local immunomodulatory applications. Hence, here we sought to investigate the ability of the NICHE technology to effectively localize the biodistribution of immunomodulating molecules and minimize systemic drug exposure. For this, we employed 3 model molecules with different molecular weights and conformations as representatives of a wide spectrum of immunomodulatory agents: CTLA4Ig (92 kDa), a clinically approved immunosuppressant, human IgG (150 kDa) as a model for monoclonal antibody-based immunosuppressants and ovalbumin (42 kDa) as a model for fusion protein antibodies with lower molecular weights. The analysis was performed in rats with NICHE implanted in the subcutaneous space, which is regarded as a promising site for cell delivery due to accessibility and minimal invasiveness. Molecules concentration was monitored longitudinally within NICHE microenvironment and surrounding tissues, in the plasma and major organs over 30 days. Characterization of tissue properties within NICHE and its surroundings, inclusive of cell, blood vessel, and collagen density was performed with emphasis on molecular transport. In this context, using fluorescence recovery after photobleaching (FRAP), we measured the effective diffusivity of the 3 molecules within relevant tissues. Finally, the data was used to develop a broadly applicable physiologically-based pharmacokinetic (PBPK) model to describe the biodistribution of molecules locally eluted via NICHE. Overall, this work provides an engineered microenvironment technology platform and framework for the development and investigation of novel local immunomodulation strategies.

2. Materials and methods

2.1. NICHE fabrication

NICHE was fabricated as previously described [37,38]. Briefly, two polyethersulfone (PES) nanoporous membranes (30 nm, Sterlitech) and two sets of nylon meshes (Elko Filtering) were affixed on the 3D printed polyamide structure (30.4 mm × 15.4 mm x 3.8 mm) with implantable grade silicone adhesive (MED3-4213, Nusil). The same adhesive was used to fabricate the silicone ports. All parts were autoclaved prior to sterile assembly under a laminar flow hood. Assembled NICHEs were sterilized at the Houston Methodist Research Institute (HMRI) Current Good Manufacturing Practice core with ethylene oxide gas.

2.2. Scanning electron microscopy (SEM) images

Nylon meshes and PES membranes were imaged with the Nova NanoSEM 230 at the HMRI SEM core. The samples were sputtered with 7 nm iridium and imaged using a 5 kV electron beam under high vacuum (10^{-3} Pa).

2.3. Animal experiments

In this study, eight-week-old male F344 rats (Charles River, Houston, TX, USA) were used. All animals were maintained and employed in conformity with guidelines established by the American Association for Laboratory Animal Science. Rats were kept in the HMRI animal facility and studies were conducted at the HMRI Comparative Medicine Program (CMP) according to provisions of the Animal Welfare Act, PHS Animal Welfare Policy, and the principles of the NIH Guide for the Care and Use of Laboratory Animals. The humane use of animals in research and all procedures detailed in the IACUC protocol number IS00005894 were approved by the Institutional Animal Care and Use Committee at HMRI. Animals were housed under standard conditions and had ad libitum access to water and a standard laboratory diet.

2.4. NICHE deployment

Sterile NICHE cell reservoir was loaded with mesenchymal stem cells (MSCs) to drive vascularization and tissue formation within the reservoir as described in our previous publications [37,38]. Briefly, a pluronic F-127 (Sigma) hydrogel (20% PF-127 in DMEM) was used to suspend F344 rat bone marrow MSCs (Cyagen). The mix was then injected into the cell reservoir of NICHEs (5×10^5 MSCs per NICHE) through the central silicone port. MSC-loaded NICHEs were implanted in a subcutaneous pocket created via a 2 cm incision in the rat dorsum, as previously described [37,38].

2.5. Histology and immunohistochemistry analysis

For histological analysis, 2, 4, and 6 weeks post-implantation, n = 4 NICHEs were explanted as a whole with the fibrotic capsule through terminal surgery. Tissues were fixed in 10% formalin for 5 days followed by dehydration in standard ethanol. NICHE polyamide structure was removed from the fixed tissue to facilitate sectioning. Dehydrated tissues were washed in xylene prior to paraffin embedding.

Hematoxylin-eosin (H&E) and Masson's Trichrome (MT) staining were performed on 5 μm sections at the HMRI Research Pathology Core. Sections scans were obtained with EVOS imaging system (Life Technologies), while magnified fields of view (FOV) were acquired with Olympus B×71 microscope equipped with Olympus DP72 camera and 40×/0.75 objective. Fibrotic capsule and skin thickness measurements were performed on MT-stained slides using ImageJ (n = 5 measurements per sample, n = 3 samples).

For immunofluorescence staining, 5 μm sections were subjected to heat-induced epitope retrieval in rodent decloaker buffer (Biocare Medical) at 121 °C for 20 min followed by blocking in 5% normal goat serum for 1 h at room temperature. Primary antibodies were incubated for 16 h at 4 °C in renaissance antibody diluent (Biocare Medical) and secondary antibodies for 1 h at room temperature in blocking buffer. Prolong Diamond mounting media with DAPI was added to preserve fluorescence (Invitrogen). Slides were visualized using FluoView 3000 confocal microscope (Olympus). Antibodies used were: alpha-smooth muscle actin (a-SMA; ab56894, Abcam), AlexaFluor 555 goat anti-rabbit (A21428, Invitrogen).

2.6. Cell, capillaries and collagen density analysis

The slides were visually divided in 4 macro-areas: Subcutaneous tissue on top of NICHE (SubQ), fibrotic capsule surrounding NICHE (Fib. Cap.), cell reservoir tissue close to the membranes (side) and tissue in the center of the cell reservoir (center).

DAPI and α-SMA stained sections were used for cell and capillary density analysis. Five FOV per macro-area were randomly acquired (n = 4 sections). Olympus cellSens software was used to automatically count DAPI-positive nuclei and to measure α-SMA-positive area. The measurements were used to calculate cell density and capillary area fraction respectively, according to the formulas below.

$$\text{Cell density} = \frac{\text{Cell count}}{\text{FOV area}} \tag{1}$$

$$\text{Capillary area fraction} = \frac{\alpha\text{-SMA-positive area}}{\text{FOV area}}*100 \tag{2}$$

MT-stained sections were used for collagen density analysis. Five FOV of each macro-area were randomly acquired (n = 4 sections). Collagen area was measured through color deconvolution followed by color thresholding using a custom Matlab script (Mathworks). Collagen density was calculated according to the formula below.

$$\text{Collagen density} = \frac{\text{Collagen-positive area}}{\text{FOV area}} \tag{3}$$

2.7. Molecules fluorescent labeling

CTLA4Ig (Orencia, Bristol-Meyers Squibb), human IgG (Sigma), and albumin from chicken egg white (Ovalbumin, Sigma) were reconstituted and conjugated to Alexa Fluor 647 NHS ester, Alexa Fluor 488 NHS ester and Alexa Fluor 568 NHS ester (Invitrogen), respectively, following the protocol provided by the manufacturer. Stock solutions for each molecule (10 mg/ml) were prepared by mixing unlabeled and Alexa Fluor-conjugated molecules at a 19:1 ratio in water for injection (USP sterile grade, RMBIO). A cocktail solution (COMBO) containing 10 mg/ml of CTLA4Ig, Human IgG and Ovalbumin was also prepared by mixing

unlabeled and Alexa Fluor-conjugated molecules at a 19:1 ratio in water for injection (USP sterile grade, RMBIO). CTLA4Ig was reconstituted and conjugated to Fluorescein-5-Isothiocyanate (FITC, Invitrogen) according to manufacturer instructions.

2.8. Tissue diffusion coefficient measurement

Vascularized NICHEs were explanted from n = 3 rats 6 weeks post-implantation. The subcutaneous tissue above the device was collected and the fibrotic capsule was dissected from the nylon mesh. Devices were sectioned in half across their width (cutting plane parallel to the ports face of the device) and the tissue contained in the cell reservoir was carefully excised. Each tissue was divided in 3 parts and placed in media (DMEM/F-12) solutions at a 2 mg/ml concentration (n = 3 set of tissues per solution) containing either CTLA4Ig-FITC, IgG-FITC (Sigma), or ovalbumin-FITC (Invitrogen), respectively. Control tissues were collected and incubated in media. After incubation overnight at 4 °C, the tissues were removed from the media solutions and placed in microscope chamber slides (Nunc Lab-Tek II, Thermofisher). The tissue diffusion coefficients of CTLA4Ig, IgG and ovalbumin were measured through FRAP method [41,42]. The cell reservoir tissues were virtually divided in 2 macro-areas: cell reservoir tissue in proximity to the drug-releasing membranes (side), and tissue in the center of the cell reservoir (center). An Olympus Fluoview 3000 microscope equipped with a 488 nm laser and a 10× objective was used to take measurements in each sample. FRAP measurements were performed as follows: 1) 3 pre-bleaching images (512 × 512 pixels) of a selected FOV were collected at low laser intensity (1%); 2) a circular area (50 pixels or 124 μm radius) was bleached by exposing it at 100% laser intensity for 100 s; 3) fluorescence recovery was detected by imaging the bleached area at low intensity for 30 min (12 images/minute).

The images were analyzed using a custom Matlab script. Briefly, the normalized fluorescent intensity measured in the bleached area over time was fitted to the following equation [43,44]:

$$f(t) = \sum_{n=0}^{n=\infty} \frac{(-b)^n}{n!} \frac{1}{1 + n\left[1 + \left(\frac{2t}{\tau_d}\right)\right]} \tag{4}$$

The bleaching parameter, b, and the characteristic diffusion time, τ_d, were fitted. τ_d was used along with the radius of the bleached area, ω, to calculate the diffusion coefficient, D, according to:

$$D = \frac{\omega^2}{4\tau_d} \tag{5}$$

2.9. Stability assessment

CTLA4Ig, IgG and Ovalbumin are dissolved in water for injection to a concentration of 2 mg/ml. Each solution is divided in n = 4 1.1 ml aliquots. One aliquot per solution is frozen at −80 °C while the others are incubated at 37 °C. After 4 and 8 weeks one aliquot per solution is removed from incubation and stored at −80 °C. Frozen aliquots are thawed and the molecules stability is assessed through gel permeation chromatography (GPC) with a Viscotek GPCmax (Malvern) equipped with a column for protein samples (P3000, Malvern). Phosphate saline buffer (PBS) with 0.02% sodium azide is used as GPC buffer.

2.10. In vivo biodistribution experiment

NICHE-MSCs were implanted in n = 32 rats. At week 6 post-implantation, the animals were randomly placed in 2 groups: a loaded group (n = 28) where NICHEs drug reservoirs were loaded with the COMBO solution, and a control group where the devices were not loaded. The loading procedure was carried out as described in our previous publications [38,45]. At day 1, 3, 6, 10, 15, 22 and 30 post drug loading,

a group of rats was euthanized (n = 4 per time-point) through CO_2 asphyxiation. After euthanasia blood was collected through cardiac puncture and NICHE was retrieved from the subcutaneous pocket. Drug reservoir content, cell reservoir tissue, fibrotic capsule, skin above the pocket, ipsilateral axillary lymph nodes, liver, kidney and spleen were collected and processed for molecules quantification.

2.11. Ex-vivo molecules concentration measurement

The tissue harvested were homogenized in T-PER buffer supplemented with protein inhibitor cocktail (Thermo Scientific). Tissue homogenates and blood were clarified via centrifugation and stored frozen until analysis.

Molecules concentration in plasma and tissue homogenates was quantified using human CTLA4 ELISA (Invitrogen), Chicken Ovalbumin ELISA (Mybiosource) and human IgG IQELISA (Raybiotech).

Drug reservoir residual concentration was measured through fluorescence using a plate reader (Synergy H4, Biotek) and analyzing the samples in duplicates.

2.12. Statistical analysis

All statistical analyses were performed using Prism 9.3.1 (Graphpad). The data is presented as mean ± standard deviation (*p < 0.05, **p < 0.01, ***p < 0.001, ****p < 0.0001).

3. Calculation

3.1. Theoretical basis of the model

Molecules are released from NICHE drug reservoir into its cell reservoir where vascularization and tissue ingrowth were driven by MSCs. The permeability and exchange surface of the nanoporous membrane control the release of molecules into the extracellular space of the cell reservoir. There, diffusion through the extracellular space allows them to reach the surrounding fibrotic capsule and subcutaneous tissue. In these areas, the molecules are cleared through the lymphatic and the vascular system at different rates based on size. The molecules are carried by the lymph flow into lymph nodes and eventually in the thoracic duct which drains in the subclavian vein. Once in the vascular network, the blood is responsible for the distribution of the molecules in major organs. The release kinetics, diffusion dynamics, and transport phenomena are described with a mechanistic approach in the PBPK model.

3.1.1. NICHE membrane permeability rate

The membrane permeability of the j-th molecule is calculated using its concentration measured in the NICHE drug reservoir residual collected during necropsy. According to Fick's law of diffusion:

$$\frac{\Delta m_j}{\Delta t * A_{\text{mem}}} = P_{\text{mem},j} * \Delta C_{kj} \tag{6}$$

where Δm_j is the difference between the molecule mass loaded in NICHE and the molecule mass measured after necropsy for the k different molecules, Δt is the time between NICHE loading and necropsy, A_{mem} is the exchange surface area of the PES membrane, $P_{\text{mem},j}$ is the membrane permeability and ΔC_j is the difference in concentration between the drug reservoir and the cell reservoir immediately after loading. The membrane permeability is derived as follows:

$$P_{\text{mem},j} = \frac{\Delta m_j}{\Delta C_j * \Delta t * A_{\text{mem}}} \tag{7}$$

The membrane permeability is used to calculate the membrane permeability rate ($k_{\text{mem},j}$) that was used in the model:

$$k_{\text{mem},j} = \frac{P_{\text{mem},j} A_{\text{mem}}}{V_{\text{dr}}} \tag{8}$$

where V_{dr} is the volume of the drug reservoir.

3.1.2. NICHE tissue diffusion rate

The tissue diffusion rate described the transport of molecules within NICHE extravascular space. In particular, we modeled the transport between the cell reservoir tissue and the fibrotic capsule ($k_{\text{fc},j}$), and between the fibrotic capsule and the surrounding subcutaneous tissue ($k_{\text{sk},j}$) as follows:

$$k_{\text{fc},j} = \frac{D_j}{x_{\text{fc}}^2} \tag{9}$$

$$k_{\text{sk},j} = \frac{D_{\text{fs},j}}{x_{\text{sk}}^2} \tag{10}$$

where D_j is the diffusion coefficient of the j-th molecule in the cell reservoir, $D_{\text{fs},j}$ is the diffusion coefficient in the fibrotic capsule and surrounding skin, x_{fc} is the characteristic diffusion length between the cell reservoir and the fibrotic capsule, and x_{sk} is the characteristic diffusion length between the fibrotic capsule and the surrounding subcutaneous tissue (Section S1.1). D_j is the average of the diffusion coefficients in the center and side macro-areas of the cell reservoir, while D_{fs} is the average of the diffusion coefficients in the fibrotic capsule and subcutaneous tissue (Section 2.8).

3.1.3. Blood vessels permeability

Molecules transport across the vascular endothelium can happen through bulk transport, when they are carried by the lymph fluid, or through diffusion. The bulk transport of molecules is size-dependent and therefore regulated by the fenestration on the blood vessels. This phenomenon is characterized by the reflection coefficient $\sigma_{i,j}$, specific for each tissue i and each molecule j, and defined by the following relation [46,47]:

$$\sigma_{i,j} = 1 - \left\{ 1 - \left[1 - \left(1 - \alpha_{i,j} \right)^2 \right]^2 \right\} G + \frac{16}{9} \alpha_{i,j}^2 \left(1 - \alpha_{i,j} \right)^2 F \tag{11}$$

where $\alpha_{i,j}$ represents the ratio between the j-th molecule hydrodynamic radius and the blood vessel pore size of the i-th organ. G and F are decreasing hydrodynamic functions (Section S1.2). Molecular extravasation driven by diffusion is described through the permeability-surface area product $P_{i,j} * S_i$, where the S_i, is calculated according to the model developed by Dogra et al. [48] (Section S1.1).

3.2. Physiologically based pharmacokinetic model development

A PBPK model was adapted to predict the local and systemic pharmacokinetics of drugs following release from NICHE (Fig. 1). The model comprises of 10 compartments, where 4 compartments represent the NICHE and its surrounding tissue (drug reservoir, cell reservoir, fibrotic capsule, and skin), 3 compartments represent the major organs (liver, spleen, kidney), and 3 compartments represent the connective tissues (lymph nodes, lymph, and blood). The various organ compartments and components of NICHE that support vascularization are modeled to contain a vascular and an extravascular sub-compartment. Vascular sub-compartments are connected to the blood compartment via blood flow (Q_i), represented by red arrows in the model schematic, while extravascular sub-compartments are connected to the lymph node via lymph flow (L_i), represented by blue arrows. The extravasation of drugs from vascular to extravascular sub-compartments is advection or diffusion-driven and is characterized by parameters defined in section 3.1.3. All vascular sub-compartments include a degradation rate constant (k_{deg}) to characterize the natural decay of molecules [49]. The various transport and physiological processes in the model are formulated as a system of
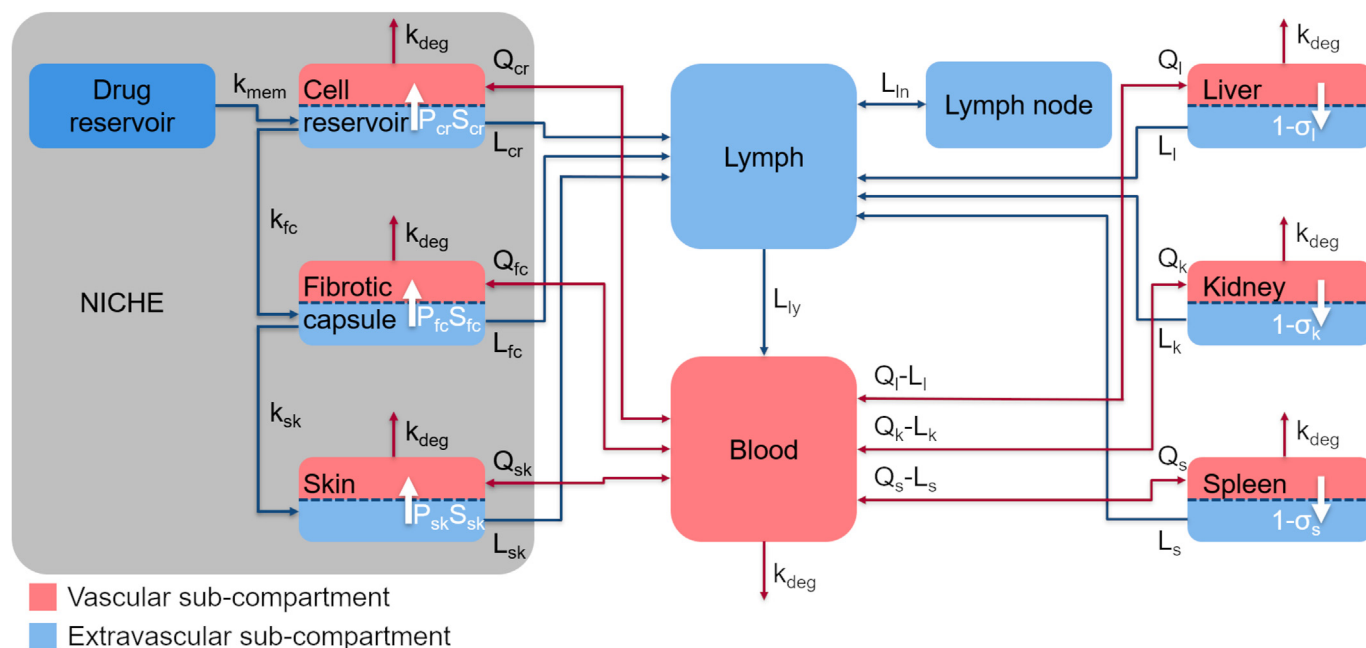
Fig. 1. PBPK model. Gray box represents the NICHE device and its neighboring tissues. Vascular compartments, sub-compartments, and their connectivity via blood are represented in red. Extravascular compartments, sub-compartments, and their connectivity are represented in light blue. Transport phenomena between sub-compartments are represented by white arrows. (For interpretation of the references to color in this figure legend, the reader is referred to the Web version of this article.)

ordinary differential equations and solved numerically as an initial value problem in Simbiology (MATLAB 2021b, Mathworks).

3.2.1. NICHE compartments

The NICHE microenvironment is described by 4 compartments: a drug reservoir compartment (dr), and 3 tissue compartments to model the cell reservoir tissue (cr), the fibrotic capsule (fc) surrounding NICHE and the skin/subcutaneous tissue above the device (sk). The drug reservoir compartment is connected to the extravascular sub-compartment of the cell reservoir to model molecular diffusion across the nanoporous membrane. The extravascular sub-compartments of cell reservoir, fibrotic capsule, and skin are sequentially connected to describe the diffusion of molecules in the extracellular space of NICHE microenvironment as defined in section 3.1.2.

3.2.2. Blood, lymph and lymph nodes compartments

The blood compartment (b) supplies blood to all vascular sub-compartments and receives the venous return from those organs, in addition to lymph (ly) drainage from the lymphatic node (ln).

3.2.3. Major organ compartments

Three compartments are used to model liver (l), spleen (s), and kidney (k), which are the major determinants of drug pharmacokinetics, especially for macromolecules.

3.2.4. Model parameters

The parameters used in the model to describe the i-th tissue and j-th molecule are obtained from the literature or derived from other mathematical models (Tables 1–4). Lymph flow values for each compartment were assumed to be 500 times smaller than the corresponding blood flow [50]. The blood vessel permeability parameters ($P_{i,j}$) and degradation rate ($k_{deg,j}$) were estimated through least square fitting.

3.2.5. Model equations

The equations representing the model are reported in Section S2 of the supplementary information.

3.3. Model parameters estimation

The unknown parameters were estimated for the 3 molecules by

Table 2
Blood, lymph and lymph node compartments parameters.

Parameter	Description (Unit)	Value			Source
		Blood (b)	Lymph (ly)	Lymph node (ln)	
V_i	Total volume (ml)	8.1	7	1	[50, 51]
L_i	Lymph flow (ml/h)	–	2.32	0.4	[50, 52]

Table 1
NICHE compartments parameters.

Parameter	Description (Unit)	Value				Source
		Drug reservoir (dr)	Cell reservoir (cr)	Fibrotic capsule (fc)	Subcutaneous tissue (sk)	
d_i	Thickness (cm)	–	0.38	0.0317	0.1872	Section 2.1, Section 2.5
V_i	Total volume (ml)	0.3	0.386	0.364	2.767	Section S1.1
$V_{i,v}$	Vascular volume (ml)	–	0.035	0.013	0.05	Section S1.1
$V_{i,e}$	Extravascular volume (ml)	–	0.128	0.12	0.915	Section S1.1
Q_i	Blood flow (ml/h)	–	7.75	2.84	1.09	Section S1.1
S_i	Vascular surface area (cm^2/cm^3)	–	362.61	141.29	72.43	Section S1.1

Table 3
Major organs compartments parameters.

Parameter	Description (Unit)	Value			Source
		Liver (l)	Spleen (s)	Kidney (k)	
V_i	Total organ volume (ml)	14	2.5	2.15	[50]
$V_{i,v}$	Organ vascular volume (ml)	1.2	0.3	0.12	[50]
$V_{i,e}$	Organ extravascular volume (ml)	2.3	0.5	0.32	[50]
Q_i	Organ blood flow (ml/h)	1044	159.82	325.89	[50, 53]
$r_{pore,i}$	Organ blood vessels fenestration radius (nm)	140	2500	7.5	[54]

fitting the model to the experimental data. The fit was performed by combining a genetic algorithm and a non-linear least square solver, using the *ga* and *lsqnonlin* functions in Simbiology.

3.4. Local sensitivity analysis

To evaluate the effect of model parameters on drug concentration in various model compartments, we performed a local sensitivity analysis,

where we evaluated the time-dependent sensitivities of drug concentration in various model compartments with respect to initial conditions and parameter values in the model. The local sensitivity was obtained from the following equation:

$$LS_{i,j}(t,k) = \left(\frac{k}{C_{i,j}(t)} \right) \left(\frac{dC_{i,j}(t)}{dk} \right) \qquad (12)$$

where $C_{i,j}$ is the concentration of the j-th molecule in the i-th compartment and k is a parameter. The results were integrated over time to obtain a dimensionless sensitivity value.

4. Results and discussion

4.1. NICHE fabrication and tissue characterization

The NICHE device (Fig. 2A) was designed and fabricated as described in our previous publications [37,38]. The NICHE central cell reservoir is surrounded by a U-shaped drug reservoir (Fig. 2B) and enclosed within 2 overlapping sets of nylon meshes presenting different openings (Fig. 2C): the inner meshes have 300 μm × 300 μm square openings and ~120 μm threads and provides mechanical support; the outer meshes have 100 μm × 100 μm openings and finer ~80 μm threads that favors cell retention

Table 4
Molecular parameters.

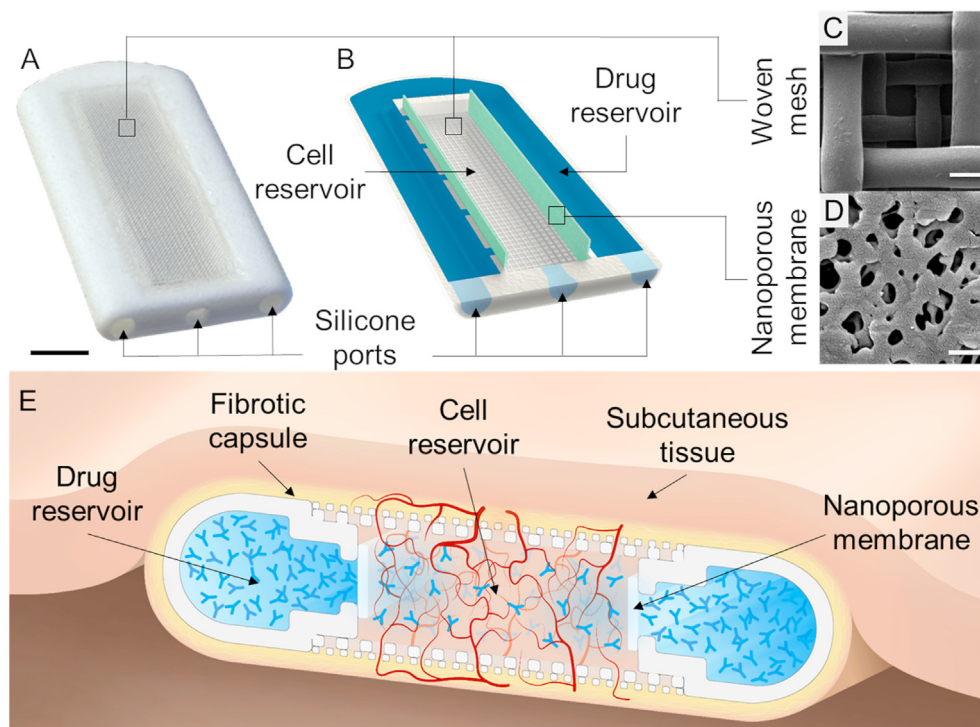| Parameter	Description (Unit)	Value			Source
		Ovalbumin	CTLA4Ig	IgG	
r_j	Radius (nm)	3.05	5.1	5.29	[55–57]
$P_{mem,j}$	Membrane permeability (cm/s)	1.67×10^{-6}	1.03×10^{-6}	7.53×10^{-7}	Section 3.1.1
$\sigma_{l,j}$	Reflection coefficient of liver (dimensionless)	0.0029	0.008	0.0086	Section 3.1.3
$\sigma_{s,j}$	Reflection coefficient of spleen (dimensionless)	9.57×10^{-6}	2.67×10^{-5}	2.87×10^{-5}	Section 3.1.3
$\sigma_{k,j}$	Reflection coefficient of kidney (dimensionless)	0.51	0.878	0.901	Section 3.1.3
D_j	Diffusion coefficient in cell reservoir (cm²/s)	11.28×10^{-8}	7.78×10^{-8}	7.39×10^{-8}	Section 3.1.2
$D_{fs,j}$	Diffusion coefficient in surrounding tissue (cm²/s)	12.67×10^{-8}	8.25×10^{-8}	8.06×10^{-8}	Section 3.1.2

Fig. 2. NICHE description. A) Picture of a fully assembled NICHE (Scale bar 5 mm). B) Rendering of longitudinal section of NICHE. C) SEM image of nylon meshes bilayer (500× magnification, scale bar 500 nm). D) SEM image of PES nanoporous membrane (50,000× magnification, scale bar 100 μm). E) Rendering of subcutaneously implanted NICHE cross section, depicting the diffusive local delivery of immunosuppressant into a vascularized cell reservoir.
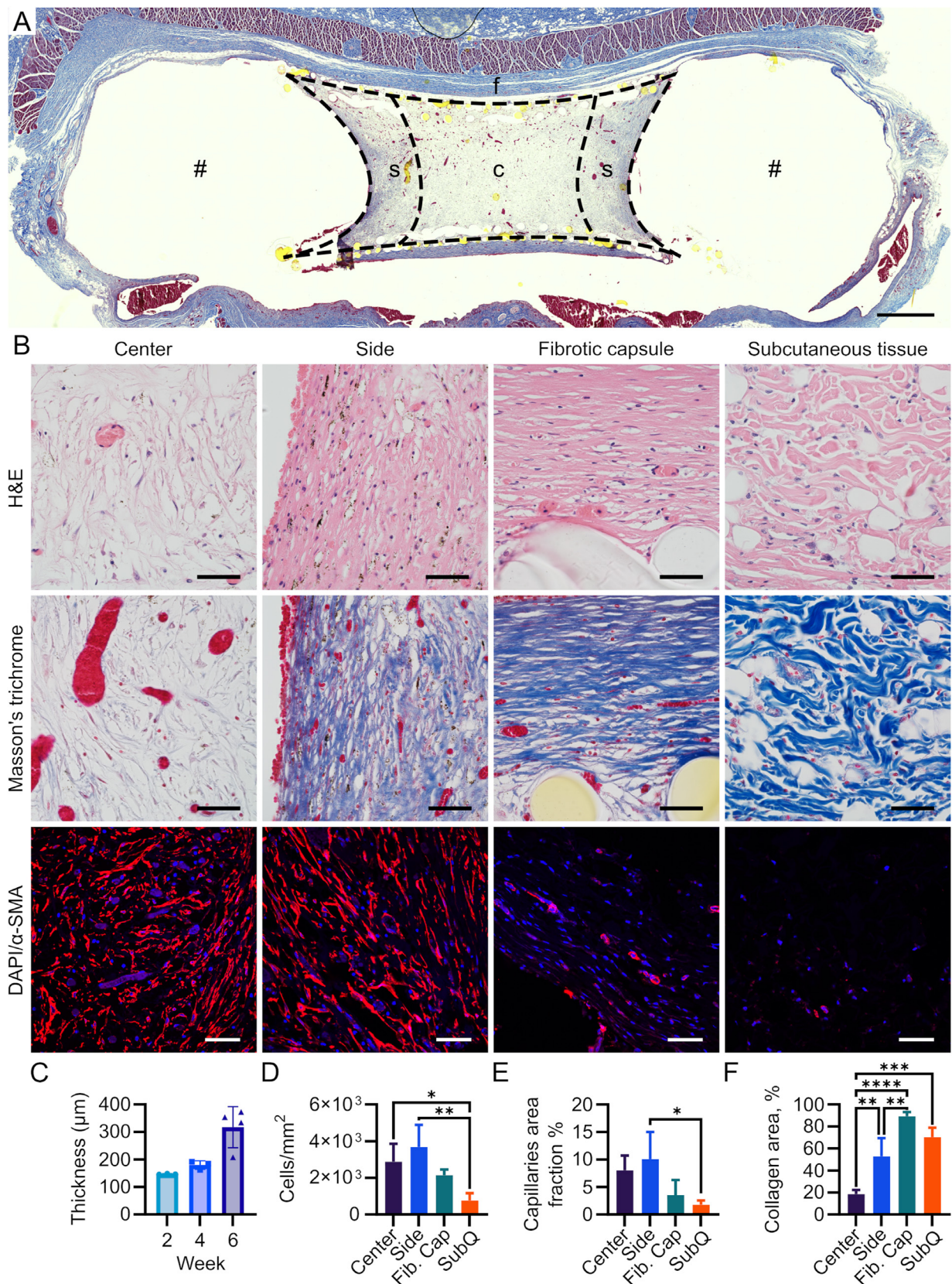
Fig. 3. NICHE tissue histology and characterization. A) Histological image of MT-stained cross section of excised NICHE tissues at week 6 post-implantation. Pound signs (#) represent the area occupied by the drug reservoir. The lines represent the division of the cell reservoir tissue in macro-areas, side (s) and center (c). The fibrotic capsule (f) is visible around the drug reservoir (Scale bar 1 mm). B) 40× magnifications of H&E, MT and DAPI and α-SMA stained NICHE cell reservoir scans (Scale bars 50 μm) explanted at week 6 post-implantation. C) Fibrotic capsule measurements over time. Quantification of D) cell density, E) capillaries area fraction and F) collagen area fraction in NICHE tissues at week 6 post-implantation.

while permitting vascular and tissue ingrowth. Upon subcutaneous implantation of MSC-loaded NICHE, tissue and neovasculature progressively penetrate across the meshes, filling and engrafting the cell reservoir within 3–4 weeks [37,45]. Long-acting sustained drug elution from the drug reservoir to the vascularized tissue in the cell reservoir is accomplished for months via a nanoporous membrane (Fig. 2D and E). As previously shown, long term deployment of the platform can be achieved via straightforward drug and cell replenishment with transcutaneous injections through the silicone ports [37].

Histological sections obtained from NICHE devices explanted 6 weeks post-implantation revealed a thin fibrotic capsule surrounding the device (Fig. 3A). The tissue penetrating the cell reservoir presented higher density in proximity of the membrane (Fig. 3A and B). Fibrotic capsule thickness increased over time up to 317 ± 64 µm at week 6 (Fig. 3C). Image analysis of sections stained with DAPI and α-SMA indicates increased cell density within NICHE cell reservoir as compared to subcutaneous tissue (Fig. 3B). Moreover, vascular-area fraction measurements showed higher blood vessels density in the cell reservoir compared to both fibrotic capsule and subcutaneous tissue (Fig. 3E). In contrast, higher density of collagen was observed in the fibrotic capsule and subcutaneous tissue than in the NICHE cell reservoir (Fig. 3F). As demonstrated in our previous work, tissue growth within the NICHE is

influenced by the MSCs retained in the cell reservoir [37,45], which are known to secrete anti-inflammatory and pro-angiogenic factors [58–61]. In fact, lower collagen deposition in the cell reservoir compared to the fibrotic capsule is indicative of the local MSC mitigation of inflammatory foreign body response [62]. Interestingly, tissue adjacent to the membrane showed increased collagen density compared to the tissue in the center of the cell reservoir. Finally, dense vascularization was observed in the cell reservoir, attributable to the angiogenic effect of MSCs, which is congruent with our previous findings [37,45].

The tissue formed in the cell reservoir showed distinct histological characteristics compared to unaltered subcutaneous tissue. To this extent, diffusion dynamics of molecules within this space were characterized via FRAP (Fig. 4A). Fluorescence recovery curves indicated a faster recovery in the central macro-area compared to the one adjacent to the membrane (Fig. 4B–D), in agreement with the histological observations. The diffusion coefficients, calculated through fitting of the recovery curves of each molecule, decreased in correspondence to the increase in respective hydrodynamic diameters (Fig. 4E). Furthermore, this behavior was visually confirmed by the shorter recovery time of ovalbumin compared to CTLA4Ig and IgG (Fig. 4A–S1). Interestingly, cell reservoir diffusion coefficients were comparable to the ones calculated for the subcutaneous tissue.
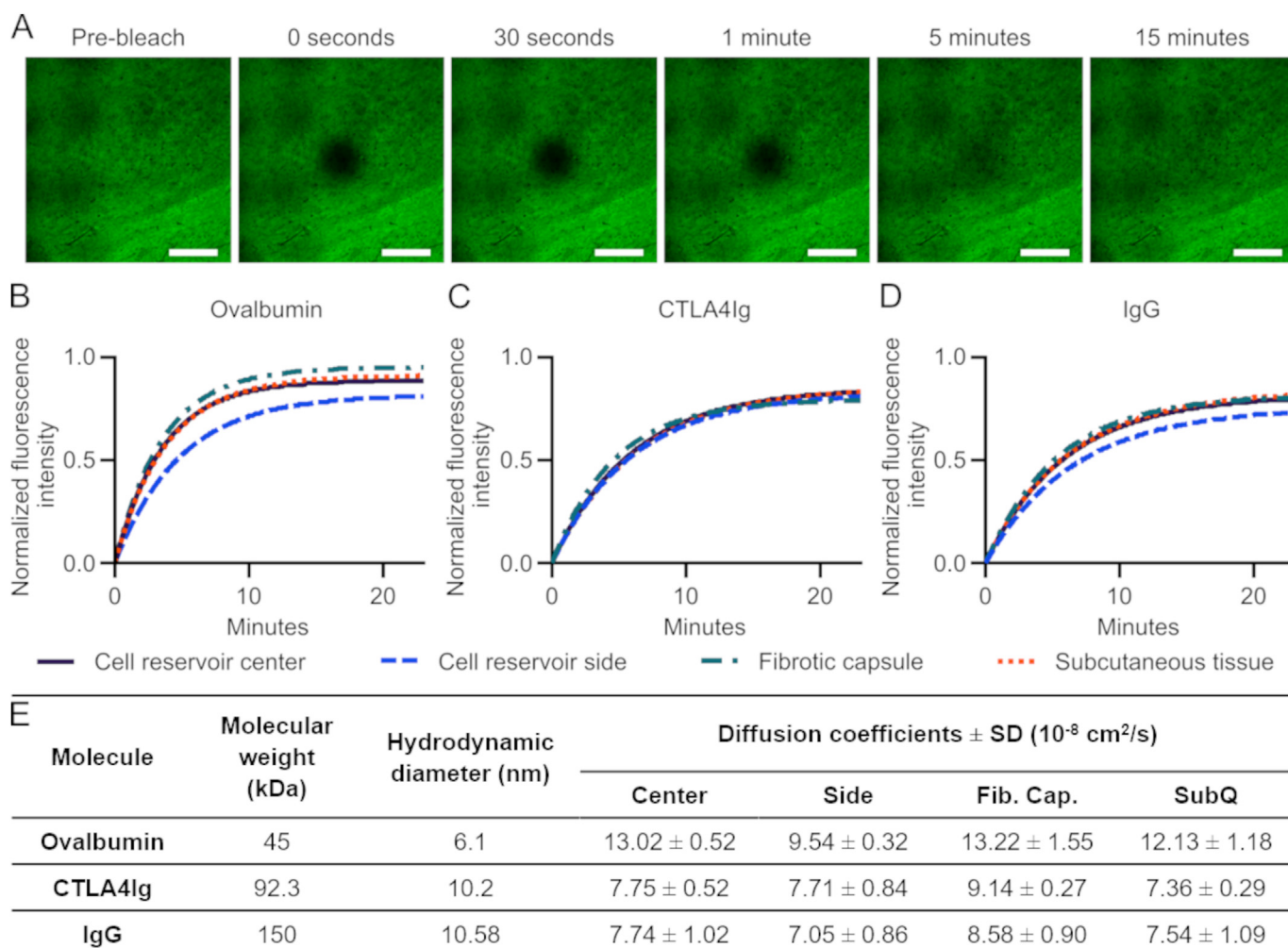

E Molecule	Molecular weight (kDa)	Hydrodynamic diameter (nm)	Diffusion coefficients $\pm$ SD (10^{-8} cm²/s)			
			Center	Side	Fib. Cap.	SubQ
Ovalbumin	45	6.1	13.02 ± 0.52	9.54 ± 0.32	13.22 ± 1.55	12.13 ± 1.18
CTLA4Ig	92.3	10.2	7.75 ± 0.52	7.71 ± 0.84	9.14 ± 0.27	7.36 ± 0.29
IgG	150	10.58	7.74 ± 1.02	7.05 ± 0.86	8.58 ± 0.90	7.54 ± 1.09

Fig. 4. Diffusion coefficient measurement in NICHE tissues. A) Representative FRAP imaging sequence of the cell reservoir center saturated with CTLA4Ig-FITC (Scale bar 300 µm). Recovery curves of B) ovalbumin, C) CTLA4Ig, D) IgG in center, side, fibrotic capsule and subcutaneous tissue macro-areas. No measurable fluorescent signal was observed in control tissues. E. Molecule sizes and calculated diffusion coefficients.

4.2. Biodistribution of molecules locally released via NICHE

The stability of the molecules was verified for at least 8 weeks under physiological conditions. All molecules showed no signs of degradation, making them suitable for a long-term biodistribution study (Fig. S2). Molecule concentrations measured in various organs and tissues after euthanasia were used to assess their biodistribution. The calculated cumulative molecules release from the drug reservoir showed a steady sustained trend (Fig. 5A–C). The daily release was estimated through linear regression. Ovalbumin, CTLA4Ig and IgG were released at a rate of 1.98%, 1.71%, 1.7% per day, respectively, indicating a size dependent behavior. IgG showed higher concentration in the cell reservoir compared to the other molecules, probably due to its larger size, which slowed down its clearance (Fig. 5D). Ovalbumin levels in lymph nodes were similar to the other molecules (Fig. 5E), however, in plasma its concentration was 10-fold lower. Interestingly, in kidneys, ovalbumin levels were consistently higher than CTLA4Ig and IgG, indicating some degree of accumulation (Fig. 5F). This difference can be explained by the glomerular barrier cut-off size observed in kidneys that allows for the filtration and subsequent elimination of particles smaller than 6–8 nm in diameter [63]. CTLA4Ig and IgG hydrodynamic diameters are both larger than the cut-off (Table 4) and therefore are retained in circulation. Differently, the size of ovalbumin (6.1 nm in diameter) allows penetration into the glomerular barrier followed by capture in the proximal tubules [64]. CTLA4Ig and IgG concentrations measured in plasma, axillary lymph nodes and major organs were about 100-folds lower compared to the cell reservoir. Furthermore, the measurements in cell reservoir, fibrotic capsule and skin showed a gradient-like decrease in concentration that points to a predominantly diffusive transport in the space surrounding the NICHE (Fig. 5G–I).

Overall, this data suggests a biodistribution mostly localized within NICHE, especially for large molecules. Furthermore, the residual molecules in the drug reservoir at day 30 were at least 30% of the loaded dose, indicating the potential of the platform for long term deployment.
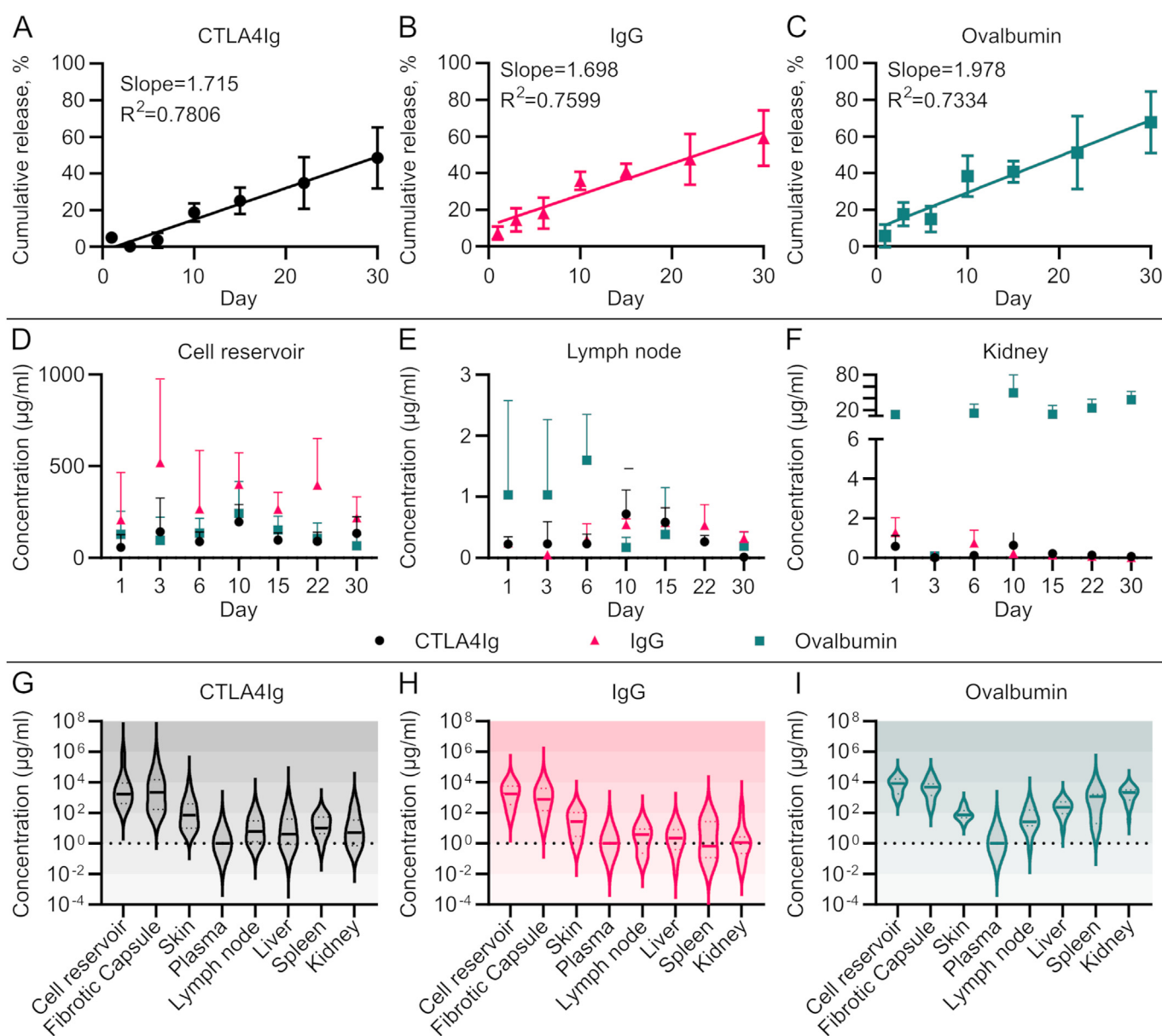

Fig. 5. In vivo molecules biodistribution. Calculated cumulative release from the drug reservoir of A) CTLA4Ig, B) IgG and C) ovalbumin. D) Cell reservoir, E) lymph nodes and F) kidney molecules concentration over time. Violin plot of tissue concentrations measured throughout 30 days normalized to plasma of G) CTLA4Ig, H) IgG and I) ovalbumin.

4.3. PBPK model fitting

The concentrations in blood, lymph node, and NICHE compartments were in good agreement with experimental measurements of the CTLA4Ig biodistribution dataset, while levels in major organs were slightly underestimated (Fig. 6). The Pearson correlation coefficient (r = 0.9903) and weighted residuals analysis however demonstrate goodness of fit; it also highlights that the underestimation occurred mostly for concentrations below 1 μg/ml (Fig. S3A). The values in the correlation plot were equally distributed around the identity line (Fig. S3B).

Similarly, the IgG concentration data were well fitted by the model despite the large variability in measured plasma levels (Fig. 7). Low concentrations were slightly underestimated, according to the weighted residual plot (Fig. S4A). For this dataset, the correlation plot showed values evenly spread around the identity line (Fig. S4B), resulting in a Pearson correlation coefficient comparable to the one obtained for CTLA4Ig (r = 0.9859).

The fitting of the ovalbumin dataset was optimal in the NICHE compartments (Fig. 8). However, the model overestimated the concentrations in the blood compartment and noticeably underestimated the major organ compartments, especially the kidney. This behavior was reflected in the weighted residual and correlation plots (Figs. S5A–B), which resulted in a slightly lower, but still acceptable, Pearson correlation coefficient (r = 0.9820). Overall, the model obeys the principle of conservation of mass and the total mass decreases over time in accordance with the experimental data (Fig. S6).

The fitting estimated permeability coefficients showed a decreasing trend with increasing molecule size, with the exception of the IgG skin and CTLA4Ig fibrotic capsule permeability coefficients (Table 5).

Notably, the model adequately estimated the concentrations in the NICHE compartments and performed well in describing plasma and lymph node levels for all 3 molecules. However, the model could not accurately represent the ovalbumin kidney tubular capture, resulting in discrepant concentrations in the compartment.

4.4. Local sensitivity analysis

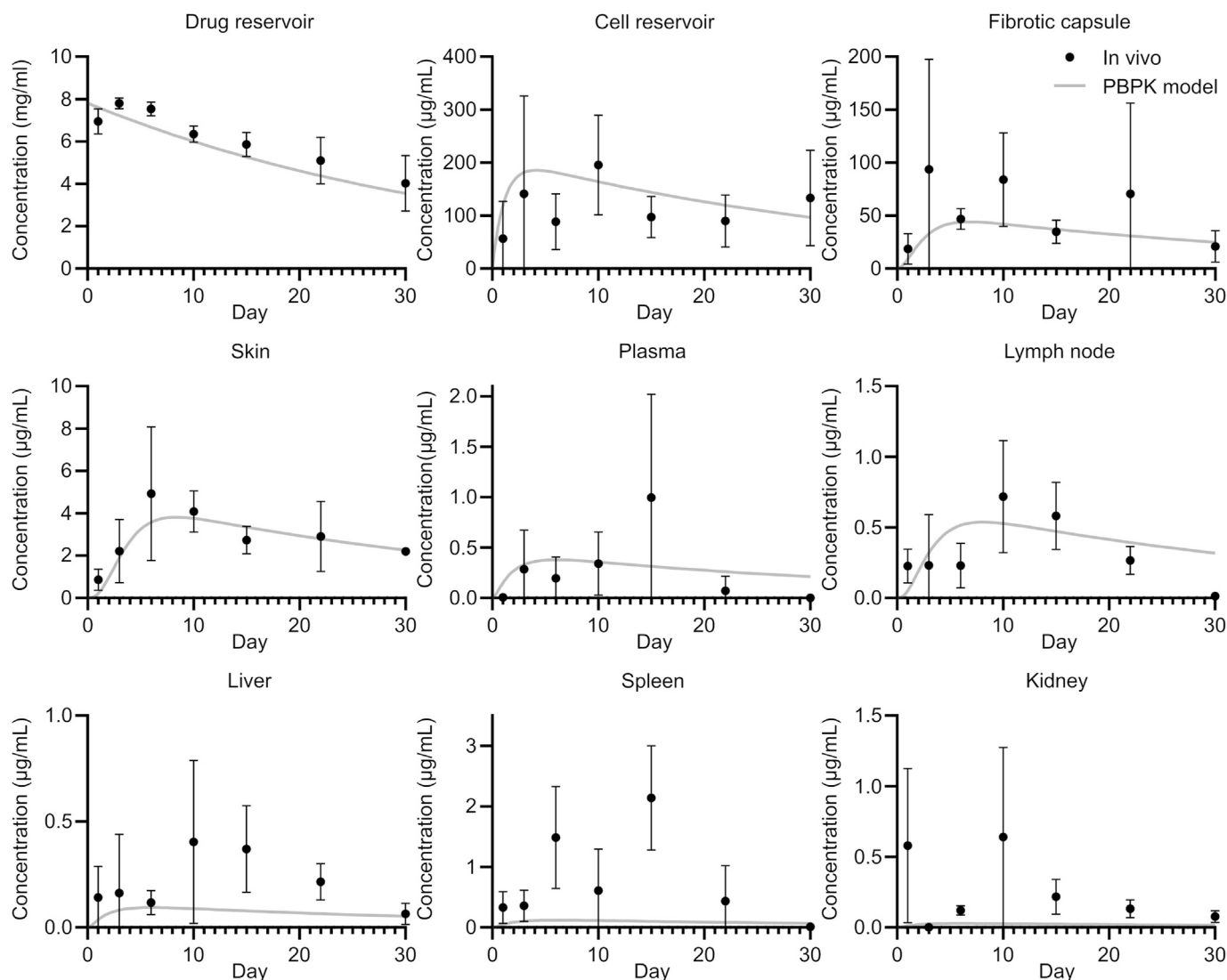We evaluated the effect of membrane parameters, permeability,

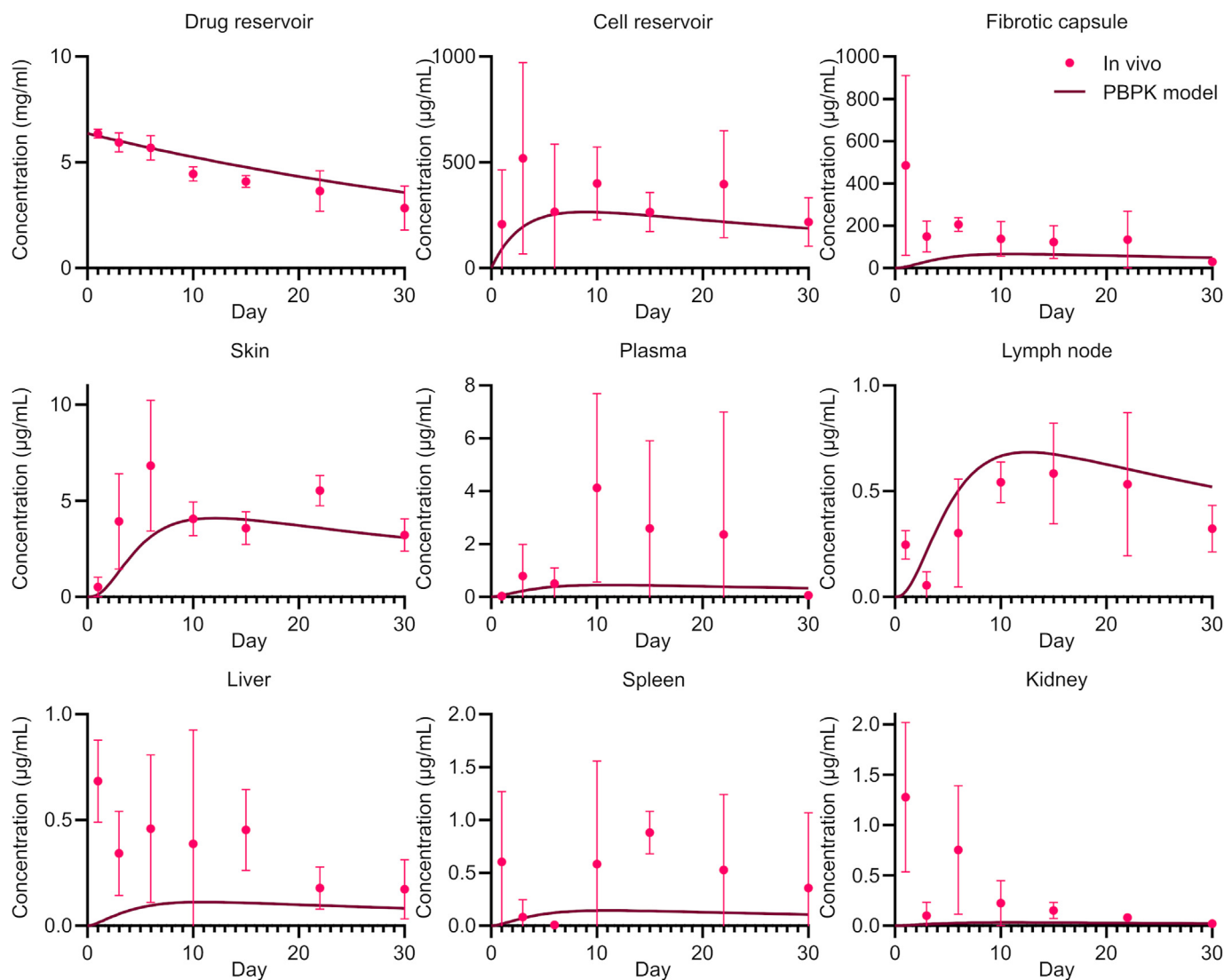**Fig. 6.** PBPK model fitted to CTLA4Ig biodistribution data.

Fig. 7. PBPK model fitted to IgG biodistribution data.

Table 5
Estimated parameters.

Parameter	Description (Unit)	Molecule		
		Ovalbumin	CTLA4Ig	IgG
$P_{cr,j}$	Permeability coefficient (cm/h)	8×10^{-5}	7×10^{-5}	1×10^{-5}
$P_{fc,j}$	Permeability coefficient (cm/h)	1×10^{-7}	1×10^{-5}	1×10^{-8}
$P_{sk,j}$	Permeability coefficient (cm/h)	3×10^{-3}	5×10^{-4}	7×10^{-4}
$k_{deg,j}$	Degradation coefficient (ml/h)	35	14	10

diffusion and degradation coefficients on the levels of molecules in various compartments (Fig. 9). Membrane permeability (P_{mem}) and exchange area (A_{mem}) moderately affected the concentration of molecules in all the compartments. Aside from a predictable impact on the NICHE compartments, the cell reservoir permeability coefficient (P_{cr}) had an effect on molecule levels in the lymph node. In fact, an increase in

permeability of cell reservoir capillaries will lead to reduced drug absorption in the lymphatic system. Furthermore, the diffusion coefficients (D, D_{fs}) had an important influence on the molecule concentrations in fibrotic capsule and subcutaneous tissue. Additionally, the levels in plasma and major organs were significantly impacted by the degradation coefficient (k_{deg}), similar to that reported by Shah and Betts [50].

5. Conclusion

In this work, we investigated the localization of PK and biodistribution of model molecules representative of immunomodulatory agents in a bioengineered neovascularized subcutaneous microenvironment within a 3D-printed cell delivery platform. Our results highlight that localization of drugs within a densely vascularized environment with minimal systemic exposure is feasible. This is highly relevant in the context of innovative strategies leveraging local manipulation of immune cells for the prevention, management and treatment of medical conditions. The good agreement between PBPK model and experimental results indicate that local and systemic drug concentration are predictable. Overall, we highlight the potential of the NICHE and the PBPK model to
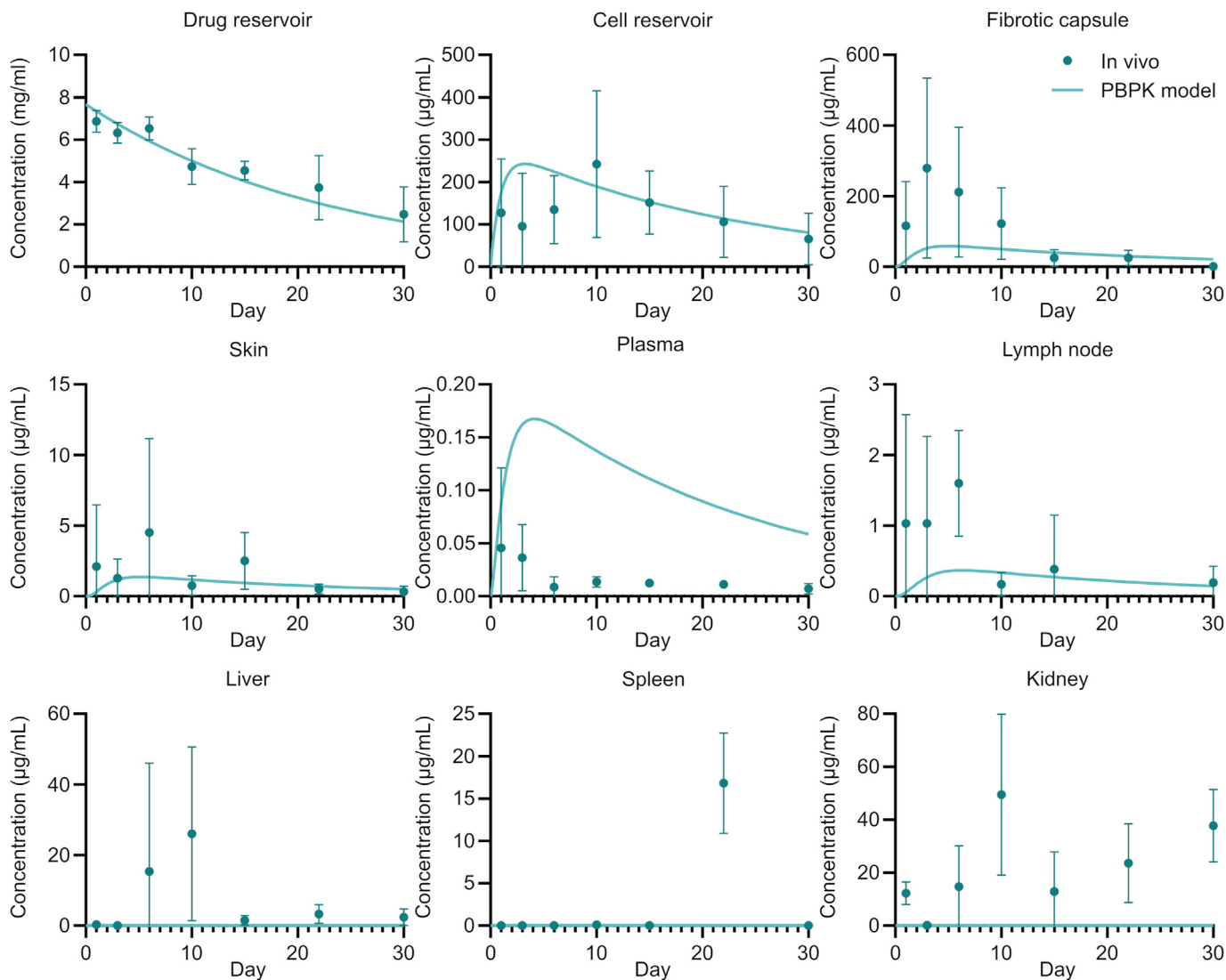
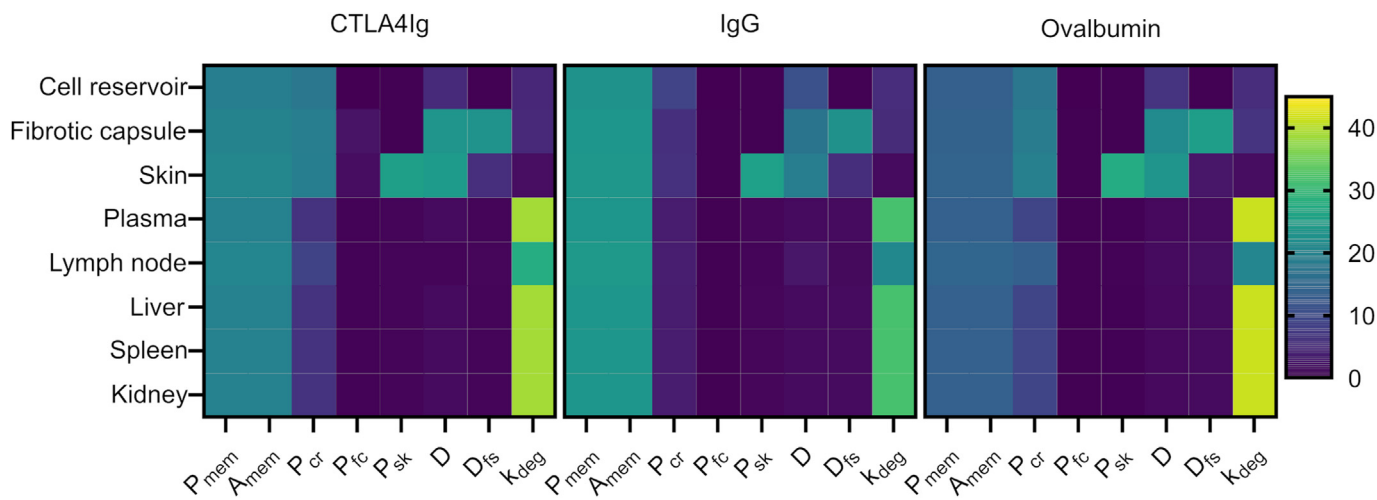**Fig. 8.** PBPK model fitted to ovalbumin biodistribution data.

Fig. 9. Sensitivity analysis. Sensitivity analysis of the CTLA4Ig, IgG and ovalbumin models. The scalebar represents the dimensionless integrated sensitivity.

serve as a foundation for the investigation and development of innovative local immunomodulatory technologies.

Data availability

The data used to support the findings of this study are available from the corresponding author upon request.

Credit author statement

SC: Conceptualization, Methodology, Validation, Formal analysis, Investigation, Data curation, Writing – original draft, Visualization. NH: Investigation. JPM: Investigation PD: Validation, Writing – review & editing. ZW: Validation. VC: Validation. CYXC: Writing – review & editing, Supervision. JEN: Writing – review & editing, Supervision. AG: Conceptualization, Writing – review & editing, Supervision, Funding acquisition.

Declaration of competing interest

The authors declare the following financial interests/personal relationships which may be considered as potential competing interests:Alessandro Grattoni reports financial support was provided by JDRF. Alessandro Grattoni reports financial support was provided by Vivian L Smith Foundation. Zhihui Wang reports financial support was provided by National Institute of Health. Vittorio Cristini reports financial support was provided by National Institutes of Health. Alessandro Grattoni has patent Transcutaneously refillable cell confinement platform with local trophic factor delivery licensed to Nanogland, Inc. Simone Capuani has patent Transcutaneously refillable cell confinement platform with local trophic factor delivery licensed to Nanogland, Inc. Jesus Paez-Mayorga has patent Transcutaneously refillable cell confinement platform with local trophic factor delivery licensed to Nanogland, Inc. Corrine Ying Xuan Chua has patent Transcutaneously refillable cell confinement platform with local trophic factor delivery licensed to Nanogland, Inc.

Appendix A. Supplementary data

Supplementary data to this article can be found online at https://doi.org/10.1016/j.mtbio.2022.100390.

References

[1] M.M. Hafiz, et al., Immunosuppression and procedure-related complications in 26 patients with type 1 diabetes mellitus receiving allogeneic islet cell transplantation, Transplantation 80 (12) (Dec 27 2005) 1718–1728, https://doi.org/10.1097/01.tp.0000187881.97068.77.

[2] N. Bulatova, A.-M. Yousef, G. Al-Khayyat, H. Qosa, Adverse effects of tacrolimus in renal transplant patients from living donors, Curr. Drug Saf. 6 (1) (2011) 3–11, https://doi.org/10.2174/157488611794480043.

[3] T.H. Tung, Tacrolimus (FK506): safety and applications in reconstructive surgery, Hand 5 (1) (Mar 2010) 1–8, https://doi.org/10.1007/s11552-009-9193-8.

[4] T. Saffari, et al., Exploring the neuroregenerative potential of tacrolimus, Expet Rev. Clin. Pharmacol. 12 (11) (Nov 2019) 1047–1057, https://doi.org/10.1080/17512433.2019.1675507.

[5] K. Griva, H.L.M. Neo, A. Vathsala, Unintentional and intentional non-adherence to immunosuppressive medications in renal transplant recipients, Int. J. Clin. Pharm. 40 (5) (Oct 2018) 1234–1241, https://doi.org/10.1007/s11096-018-0652-6.

[6] S. Duncan, R. Annunziato, C. Dunphy, D. LaPointe Rudow, B. Shneider, E. Shemesh, A systematic review of immunosuppressant adherence interventions in transplant recipients: decoding the streetlight effect, Pediatr. Transplant. 22 (1) (Feb 2018), e13086, https://doi.org/10.1111/petr.13086.

[7] M.O. Dellacherie, B.R. Seo, D.J. Mooney, Macroscale biomaterials strategies for local immunomodulation," (in English), Nat. Rev. Mater. 4 (6) (Jun 2019) 379–397, https://doi.org/10.1038/s41578-019-0106-3.

[8] K. Adu-Berchie, D.J. Mooney, Biomaterials as local niches for immunomodulation, Acc. Chem. Res. 53 (9) (Sep 15 2020) 1749–1760, https://doi.org/10.1021/acs.accounts.0c00341 (in English).

[9] B. Davis, et al., Controlled release of FK506 from micropatterned PLGA films: potential for application in peripheral nerve repair, Neural regeneration research 13 (7) (Jul 2018) 1247, https://doi.org/10.4103/1673-5374.235063.

[10] K.J. Zuo, et al., Local FK506 drug delivery enhances nerve regeneration through fresh, unprocessed peripheral nerve allografts, Exp. Neurol. 341 (Jul 2021), 113680, https://doi.org/10.1016/j.expneurol.2021.113680 (in English).

[11] M. Farina, J.F. Alexander, U. Thekkedath, M. Ferrari, A. Grattoni, Cell encapsulation: overcoming barriers in cell transplantation in diabetes and beyond, Adv. Drug Deliv. Rev. 139 (2019/01 2019) 92–115, https://doi.org/10.1016/j.addr.2018.04.018.

[12] B. Saleh, et al., Local immunomodulation using an adhesive hydrogel loaded with miRNA-laden nanoparticles promotes wound healing, Small 15 (36) (Sep 4 2019) 1902232, https://doi.org/10.1002/smll.201902232 (in English).

[13] M. Kharaziha, A. Baidya, N. Annabi, Rational design of immunomodulatory hydrogels for chronic wound healing, Adv. Mater. 33 (39) (Oct 2021) 2100176, https://doi.org/10.1002/adma.202100176.

[14] S. Capuani, G. Malgir, C.Y.X. Chua, A. Grattoni, Advanced strategies to thwart foreign body response to implantable devices, Bioengineering & Translational Medicine (Mar 2 2022), e10300, https://doi.org/10.1002/btm2.10300 (in English).

[15] D.I. Viswanath, H.-C. Liu, D.P. Huston, C.Y.X. Chua, A. Grattoni, Emerging biomaterial-based strategies for personalized therapeutic in situ cancer vaccines, Biomaterials 280 (Jan 2022), 121297, https://doi.org/10.1016/j.biomaterials.2021.121297.

[16] D.I. Viswanath, et al., Engineered implantable vaccine platform for continuous antigen-specific immunomodulation, Biomaterials 281 (Feb 2022), 121374, https://doi.org/10.1016/j.biomaterials.2022.121374.

[17] H. Phuengkham, C. Song, S.H. Um, Y.T. Lim, Implantable synthetic immune niche for spatiotemporal modulation of tumor-induced immunosuppression and systemic antitumor immunity: postoperative immunotherapy, Adv. Mater. 30 (18) (May 2018), 1706719, https://doi.org/10.1002/adma.201706719.

[18] Q. Fan, et al., An implantable blood clot–based immune niche for enhanced cancer vaccination, Sci. Adv. 6 (39) (Sep 2020) eabb4639, https://doi.org/10.1126/sciadv.abb4639.

[19] S.C. Balmert, C. Donahue, J.R. Vu, G. Erdos, L.D. Falo Jr., S.R. Little, In vivo induction of regulatory T cells promotes allergen tolerance and suppresses allergic contact dermatitis, J. Contr. Release 261 (Sep 10 2017) 223–233, https://doi.org/10.1016/j.jconrel.2017.07.006.

[20] M.-J. Sun, Z. Teng, P.-S. Fan, X.-G. Chen, Y. Liu, Bridging micro/nano-platform and airway allergy intervention, J. Contr. Release 341 (Jan 2022) 364–382, https://doi.org/10.1016/j.jconrel.2021.11.040.

[21] S. Goel, et al., Sequential deconstruction of composite drug transport in metastatic breast cancer, Sci. Adv. 6 (26) (2020) eaba4498, https://doi.org/10.1126/sciadv.aba4498.

[22] S. Goel, et al., Size-optimized Ultrasmall porous silica nanoparticles depict vasculature-based differential targeting in triple negative breast cancer, Small 15 (46) (2019), 1903747, https://doi.org/10.1002/smll.201903747.

[23] P. Dogra, et al., Mathematical modeling in cancer nanomedicine: a review, Biomed. Microdevices 21 (2) (Apr 4 2019) 1–23, https://doi.org/10.1007/s10544-019-0380-2.

[24] S. Wilhelm, et al., Analysis of nanoparticle delivery to tumours, Nat. Rev. Mater. 1 (5) (May 2016) 1–12, https://doi.org/10.1038/natrevmats.2016.14.

[25] P. Kuppan, et al., Co-localized immune protection using dexamethasone-eluting micelles in a murine islet allograft model, Am. J. Transplant. 20 (3) (Mar 2020) 714–725, https://doi.org/10.1111/ajt.15662.

[26] S. Rahimian, M.F. Fransen, J.W. Kleinovink, M. Amidi, F. Ossendorp, W.E. Hennink, Polymeric microparticles for sustained and local delivery of antiCD40 and antiCTLA-4 in immunotherapy of cancer, Biomaterials 61 (Aug 2015) 33–40, https://doi.org/10.1016/j.biomaterials.2015.04.043.

[27] M.R. Haque, D.Y. Lee, C.-H. Ahn, J.-H. Jeong, Y. Byun, Local co-delivery of pancreatic islets and liposomal clodronate using injectable hydrogel to prevent acute immune reactions in a type 1 diabetes, Pharmaceut. Res. 31 (9) (Sep 2014) 2453–2462, https://doi.org/10.1007/s11095-014-1340-4 (in English).

[28] K.W. Witwer, J. Wolfram, Extracellular vesicles versus synthetic nanoparticles for drug delivery, Nat. Rev. Mater. 6 (2) (2021) 103–106, https://doi.org/10.1038/s41578-020-00277-6.

[29] J. Wolfram, M. Ferrari, Clinical cancer nanomedicine, Nano Today 25 (2019) 85–98, https://doi.org/10.1016/j.nantod.2019.02.005.

[30] S. Pathak, et al., Single synchronous delivery of FK506-loaded polymeric microspheres with pancreatic islets for the successful treatment of streptozocin-induced diabetes in mice, Drug Deliv. 24 (1) (Nov 2017) 1350–1359, https://doi.org/10.1080/10717544.2017.1377317.

[31] K. Jiang, J.D. Weaver, Y. Li, X. Chen, J. Liang, C.L. Stabler, Local release of dexamethasone from macroporous scaffolds accelerates islet transplant engraftment by promotion of anti-inflammatory M2 macrophages, Biomaterials 114 (Jan 2017) 71–81, https://doi.org/10.1016/j.biomaterials.2016.11.004.

[32] C. Stabler, Y. Li, J. Stewart, B. Keselowsky, Engineering immunomodulatory biomaterials for type 1 diabetes, Nat. Rev. Mater. 4 (6) (Jun 2019) 429–450, https://doi.org/10.1038/s41578-019-0112-5.

[33] C.Y.X. Chua, et al., Intratumoral nanofluidic system for enhancing tumor biodistribution of agonist CD40 antibody, Advanced Therapeutics 3 (10) (Oct 2020) 2000055, https://doi.org/10.1002/adtp.202000055 (in English).

[34] H.-C. Liu, et al., Potentiating antitumor efficacy through radiation and sustained intratumoral delivery of anti-CD40 and anti-PDL1," (in English), Int. J. Radiat. Oncol. Biol. Phys. 110 (2) (Jun 1 2021) 492–506, https://doi.org/10.1016/j.ijrobp.2020.07.2326.

[35] J.N. Campa-Carranza, J. Paez-Mayorga, C.Y.X. Chua, J.E. Nichols, A. Grattoni, Emerging local immunomodulatory strategies to circumvent systemic immunosuppression in cell transplantation, Expet Opin. Drug Deliv. 19 (5) (May 2022), https://doi.org/10.1080/17425247.2022.2076834 null-null.

[36] F.P. Pons-Faudoa, A. Ballerini, J. Sakamoto, A. Grattoni, Advanced implantable drug delivery technologies: transforming the clinical landscape of therapeutics for chronic diseases, Biomed. Microdevices 21 (2) (May 18 2019) 47, https://doi.org/10.1007/s10544-019-0389-6.

[37] J. Paez-Mayorga, et al., Neovascularized implantable cell homing encapsulation platform with tunable local immunosuppressant delivery for allogeneic cell transplantation, Biomaterials 257 (2020/10 2020), 120232, https://doi.org/10.1016/j.biomaterials.2020.120232.

[38] J. Paez-Mayorga, et al., Implantable niche with local immunosuppression for islet allotransplantation achieves type 1 diabetes reversal, Preprint (2022), https://doi.org/10.21203/rs.3.rs-1285406/v1.

[39] M. Farina, et al., Transcutaneously refillable, 3D-printed biopolymeric encapsulation system for the transplantation of endocrine cells, Biomaterials 177 (2018/09 2018) 125–138, https://doi.org/10.1016/j.biomaterials.2018.05.047.

[40] A. Grattoni, S. Capuani, and J. Paez-Mayorga, "Transcutaneously refillable cell confinement platform with local trophic factor delivery. U.S. Provisional Pat. Ser. No. 63/043,439. June 24, 2020," Patent Appl. 63/043,439, 2020.

[41] D. Axelrod, D. Koppel, J. Schlessinger, E. Elson, W.W. Webb, Mobility measurement by analysis of fluorescence photobleaching recovery kinetics, Biophys. J. 16 (9) (Sep 1976) 1055–1069, https://doi.org/10.1016/S0006-3495(76)85755-4.

[42] J. Blonk, A. Don, H. Van Aalst, J. Birmingham, Fluorescence photobleaching recovery in the confocal scanning light microscope," (in English), J. Microsc. 169 (3) (Mar 1993) 363–374, https://doi.org/10.1111/j.1365-2818.1993.tb03312.x.

[43] P.A. Perry, M.A. Fitzgerald, R.G. Gilbert, Fluorescence recovery after photobleaching as a probe of diffusion in starch systems, Biomacromolecules 7 (2) (Feb 2006) 521–530, https://doi.org/10.1021/bm0507711 (in English).

[44] M.C. Branco, D.J. Pochan, N.J. Wagner, J.P. Schneider, Macromolecular diffusion and release from self-assembled β-hairpin peptide hydrogels, Biomaterials 30 (7) (Mar 2009) 1339–1347, https://doi.org/10.1016/j.biomaterials.2008.11.019.

[45] J. Paez-Mayorga, et al., Enhanced in vivo vascularization of 3D-printed cell encapsulation device using platelet-rich plasma and mesenchymal stem cells, Advanced Healthcare Materials 9 (19) (2020), 2000670, https://doi.org/10.1002/adhm.202000670.

[46] M. Mescam, P.A. Eliat, C. Fauvel, J.D.d. Certaines, J. Bézy-Wendling, A physiologically based pharmacokinetic model of vascular–extravascular exchanges during liver carcinogenesis: application to MRI contrast agents, Contrast Media Mol. Imaging 2 (5) (Sep-Oct 2007) 215–228, https://doi.org/10.1002/cmmi.147.

[47] B. Rippe, B. Haraldsson, Transport of macromolecules across microvascular walls: the two-pore theory, Physiol. Rev. 74 (1) (Jan 1994) 163–219, https://doi.org/10.1152/physrev.1994.74.1.163.

[48] P. Dogra, et al., A mathematical model to predict nanomedicine pharmacokinetics and tumor delivery, Comput. Struct. Biotechnol. J. 18 (2020) 518–531, https://doi.org/10.1016/j.csbj.2020.02.014.

[49] L. Fronton, S. Pilari, W. Huisinga, Monoclonal antibody disposition: a simplified PBPK model and its implications for the derivation and interpretation of classical compartment models, J. Pharmacokinet. Pharmacodyn. 41 (2) (Apr 2014) 87–107, https://doi.org/10.1007/s10928-014-9349-1.

[50] D.K. Shah, A.M. Betts, Towards a platform PBPK model to characterize the plasma and tissue disposition of monoclonal antibodies in preclinical species and human, J. Pharmacokinet. Pharmacodyn. 39 (1) (Feb 2012) 67–86, https://doi.org/10.1007/s10928-011-9232-2.

[51] D. Sugasini, V. Devaraj, M. Ramesh, B. Lokesh, Lymphatic transport of α-linolenic acid and its conversion to long chain n-3 fatty acids in rats fed microemulsions of linseed oil, Lipids 49 (3) (Mar 2014) 225–233, https://doi.org/10.1007/s11745-013-3873-4.

[52] M. Ionac, One technique, two approaches, and results: thoracic duct cannulation in small laboratory animals, Microsurgery 23 (3) (2003) 239–245, https://doi.org/10.1002/micr.10136.

[53] M. Daemen, et al., Liver blood flow measurement in the rat the electromagnetic versus the microsphere and the clearance methods, J. Pharmacol. Methods 21 (4) (Jul 1989) 287–297, https://doi.org/10.1016/0160-5402(89)90066-1.

[54] H. Sarin, Physiologic upper limits of pore size of different blood capillary types and another perspective on the dual pore theory of microvascular permeability, Journal of angiogenesis research 2 (1) (2010) 1–19, https://doi.org/10.1186/2040-2384-2-14.

[55] H.P. Erickson, Size and shape of protein molecules at the nanometer level determined by sedimentation, gel filtration, and electron microscopy, Biol. Proced. Online 11 (1) (Dec 2009) 32–51, https://doi.org/10.1007/s12575-009-9008-x.

[56] J.L. Fast, A.A. Cordes, J.F. Carpenter, T.W. Randolph, Physical instability of a therapeutic Fc fusion protein: domain contributions to conformational and colloidal stability, Biochemistry 48 (49) (Dec 15 2009) 11724–11736, https://doi.org/10.1021/bi900853v.

[57] J.K. Armstrong, R.B. Wenby, H.J. Meiselman, T.C. Fisher, The hydrodynamic radii of macromolecules and their effect on red blood cell aggregation, Biophys. J. 87 (6) (Dec 2004) 4259–4270, https://doi.org/10.1529/biophysj.104.047746.

[58] M.F. Pittenger, D.E. Discher, B.M. Peault, D.G. Phinney, J.M. Hare, A.I. Caplan, Mesenchymal stem cell perspective: cell biology to clinical progress, NPJ Regen Med 4 (2019) 22, https://doi.org/10.1038/s41536-019-0083-6.

[59] H. Tao, Z. Han, Z.C. Han, Z. Li, Proangiogenic features of mesenchymal stem cells and their therapeutic applications, Stem Cell. Int. 2016 (2016), 1314709, https://doi.org/10.1155/2016/1314709.

[60] R. Guillamat-Prats, The role of MSC in wound healing, scarring and regeneration, Cells 10 (7) (Jul 8 2021) 1729, https://doi.org/10.3390/cells10071729.

[61] J.E. Nichols, et al., Neurogenic and neuro-protective potential of a novel subpopulation of peripheral blood-derived CD133+ ABCG2+CXCR4+ mesenchymal stem cells: development of autologous cell-based therapeutics for traumatic brain injury, Stem Cell Res. Ther. 4 (1) (Jan 6 2013) 3, https://doi.org/10.1186/scrt151.

[62] L.A. Ortiz, et al., Interleukin 1 receptor antagonist mediates the antiinflammatory and antifibrotic effect of mesenchymal stem cells during lung injury, Proc. Natl. Acad. Sci. USA 104 (26) (Jun 26 2007) 11002–11007, https://doi.org/10.1073/pnas.0704421104.

[63] B. Du, et al., Glomerular barrier behaves as an atomically precise bandpass filter in a sub-nanometre regime, Nat. Nanotechnol. 12 (11) (Nov 2017) 1096–1102, https://doi.org/10.1038/Nnano.2017.170.

[64] M.G. Lawrence, et al., Permeation of macromolecules into the renal glomerular basement membrane and capture by the tubules, Proc. Natl. Acad. Sci. USA 114 (11) (Mar 14 2017) 2958–2963, https://doi.org/10.1073/pnas.1616457114.